Observation of the magnetic C_4 phase in $Ca_{1-x}Na_xFe_2As_2$ and its universality in the hole-doped 122 superconductors

K. M. Taddei,[1,2,3,*] J. M. Allred,[3] D. E. Bugaris,[3] S. H. Lapidus,[4] M. J. Krogstad,[2,3] H. Claus,[3] D. Y. Chung,[3] M. G. Kanatzidis,[3,5] R. Osborn,[3] S. Rosenkranz,[3] and O. Chmaissem[2,3]

[1]*Quantum Condensed Matter Division, Oak Ridge National Laboratory, Oak Ridge, Tennessee 37831, USA*

[2]*Department of Physics, Northern Illinois University, DeKalb, Illinois 60115, USA*

[3]*Materials Science Division, Argonne National Laboratory, Argonne, Illinois 60439, USA*

[4]*Advanced Photon Source, Argonne National Laboratory, Argonne, Illinois 60439, USA*

[5]*Department of Chemistry, Northwestern University, Evanston, Illinois 60208, USA*

(Received 20 December 2016; revised manuscript received 25 January 2017; published 15 February 2017)

Since its discovery in 2014, the magnetic tetragonal C_4 phase has been identified in a growing number of hole-doped 122 Fe-based superconducting compounds. Exhibiting a unique double-**Q** magnetic structure and a strong competition with both superconducting and magnetic order parameters, the C_4 phase and the conditions of its formation are of significant interest to understanding the fundamental mechanisms in these materials. Particularly, separating the importance of direct changes to the relative size of hole and electron pockets at the Fermi surface (achieved via charge doping) from the role of structural changes due to differences of ionic radii of dopants is useful to determine the underlying parameter which causes the C_4 instability. Here, we report the discovery of the C_4 phase in a fourth member of the hole-doped 122 materials $Ca_{1-x}Na_xFe_2As_2$ ($0.20 \leqslant x \leqslant 0.50$) as determined from neutron and x-ray powder diffraction studies. The maximum of the C_4 dome is observed at $x = 0.44$ with a reentrant temperature $T_r = 52$ K and an extent of $\Delta x \sim 0.07$ in composition. It is observed that for a range of compositions within the C_4 dome ($0.40 \leqslant x \leqslant 0.42$), there is a second reentrance ($T_{r_2} < T_r$) where the antiferromagnetic C_2 phase is recovered—a feature previously only seen in $Ba_{1-x}K_xFe_2As_2$. A phase diagram is presented for $Ca_{1-x}Na_xFe_2As_2$ and compared to the other Na-doped 122's—$A_{1-x}Na_xFe_2As_2$ with A = Ba, Sr, and Ca. The structural parameters for these three systems are compared and the importance of the "chemical pressure" due to changing the A-site ion (A = Ba, Sr, Ca) is discussed.

DOI: 10.1103/PhysRevB.95.064508

I. INTRODUCTION

Since their discovery in 2006, there has been a debate about the Fe-based superconductors (FBS) over whether a spin/itinerant or localized orbital treatment is the appropriate model for their electronic behavior [1]. Despite similarities to the well-studied cuprate superconductors which might suggest a localized picture, behaviors such as "poor-metal" properties (rather than Mott insulating), Fermi surface (FS) nesting driven spin-density wave (SDW) magnetic ordering, and strong magnetoelastic coupling indicate the importance of itinerant spin dynamics in correctly describing these systems [2–5]. Indeed, measurements of different properties have found support of either model with magnetic torque, resistivity anisotropy, and orbital ordering supporting orbital mechanics, while measurements of the dynamic spin excitations, strain magnetism coupling, and magnetoelastic scaling strongly suggest a spin-driven scenario [6–11]. Yet determining the correct model, and consequently the underlying primary order parameter, is vital to understanding the mechanism of superconductivity in these systems. The recent discovery of a magnetic phase with fourfold C_4 symmetry in the hole-doped 122 FBS has evidenced the vital role of itinerant electronic behavior in determining the behavior of these materials. Furthermore, it has opened up an avenue to study the interplay of magnetism and superconductivity [12,13].

To date, the C_4 phase has been observed in three members of the hole-doped 122 family: $Ba_{1-x}Na_xFe_2As_2$, $Ba_{1-x}K_xFe_2As_2$, and, most recently, $Sr_{1-x}Na_xFe_2As_2$ [12–14]. In these materials, the typical suppression of the antiferromagnetically (AFM) ordered orthorhombic C_2 phase (so-called for the twofold rotation axis) upon doping is complicated by a reentrant tetragonal ($I4/mmm$ symmetry) magnetically reorientated C_4 phase. This higher-symmetry phase appears at temperatures (T_r) below the C_2 transition (T_N) and at compositions (x) less than or equal to the critical concentration (x_c) beyond which no ordered magnetism is observed. This describes a C_4 dome which exists near the complete suppression of the C_2 dome.

The C_4 phase inhabits a unique intersection, exhibiting not only an exotic magnetic double-**Q** structure born of the superposition of two itinerant SDW's, but also forming in the vicinity of superconductivity. Consequently, it has become the focus of many recent first-principles reports to reveal what parameters are causing the sudden reordering of the single-**Q** C_2 structure into this double-**Q** structure and how this phase hosts superconductivity [12,15–19]. Currently, several different proposed models predict the observed C_4, but they do so through different mechanisms, which range from expanded itinerant mean-field models to impurity scattering stabilization to spin-orbit coupling driven spin anisotropies [15,17,18]. The different models invoke varying assumptions about the underlying physics in these materials and necessarily predict different, sometimes subtlety so, manifestations of the C_4 phase. It is therefore worthwhile to attempt to discern between these models in order to inform future investigations. While some of the subtler new predictions made are experimentally

*Corresponding author: taddeikm@ornl.gov

 ©2017 American Physical Society

challenging to verify, one relatively simple validation is the comparison of the predicted phase diagrams with those found experimentally—specifically in the manifestation in temperature and composition space of the C_4 phase and its competition with superconductivity and the C_2 magnetic ordering. Such comparisons help not only in discerning between different models, but also in designating possible physically realized ranges of parameters within each model.

It is therefore relevant to return to previously studied hole-doped 122's to search for the presence of the C_4 phase, whose small extent in composition is easy to miss in less exhaustive work. Such studies have so far found C_4 in both the well-studied $Ba_{1-x}K_xFe_2As_2$ and $Sr_{1-x}Na_xFe_2As_2$ materials [14,20]. The robust C_4 phase found in this latter system informs a return to the Na^+-doped $CaFe_2As_2$. Several reported phase diagrams for $Ca_{1-x}Na_xFe_2As_2$ exist, notably in Refs. [21] and [22]; however, their authors' use of large steps in composition means that any C_4 phase would likely have been missed. Furthermore, thus far no clear evidence of the C_4 phase has been reported from either magnetization or resistivity measurements indicating that even with the right compositions the phase can be missed in the absence of temperature-dependent diffraction studies. Therefore, the large number of studies on $Ca_{1-x}Na_xFe_2As_2$ which have relied on these characterization techniques would not necessarily have been sensitive to this phase reentrance [23–26].

In this paper, we determine the $Ca_{1-x}Na_xFe_2As_2$ phase diagram and present the results of a careful systematic structural and magnetic study of compositions near the suppression of the C_2 dome. Using a combination of neutron and x-ray scattering, we observe the presence of a C_4 dome in $Ca_{1-x}Na_xFe_2As_2$. We compare the $Ca_{1-x}Na_xFe_2As_2$ phase diagram to those of $Ba_{1-x}Na_xFe_2As_2$ and $Sr_{1-x}Na_xFe_2As_2$ in order to isolate the effect of lattice anisotropy and the geometry of the Fe_2As_2 layers on the formation and extent of the C_4 phase and wider features of the phase diagrams in general.

II. EXPERIMENTAL DETAILS

A. Synthesis of $Ca_{1-x}Na_xFe_2As_2$

Polycrystalline samples of $Ca_{1-x}Na_xFe_2As_2$ (with $0.20 \leqslant x \leqslant 0.50$) were synthesized by sintering stoichiometric ratios of the prereacted binary precursors CaAs, NaAs, and Fe_2As using a method similar to that reported in Ref. [20]. The intimately ground mixtures were loaded in alumina crucibles and arc welded in Nb tubes under Ar atmosphere to prevent loss of the volatile alkali metal. The welded Nb tubes were sealed inside evacuated quartz tubes and sintered at 850 °C for 48 hours. The resultant powder was ground with a mortar and pestle and then reannealed at 900 °C. Subsequent reannealings at temperatures between 900 and 950 °C with soak times between 17 and 25 hours were found necessary to ensure compositional homogeneity. Initial characterization of the dark-gray powders was conducted by laboratory powder x-ray diffraction to check phase purity and crystallinity. Magnetization measurements were conducted at 0.1 Oe on a home-built superconducting quantum interference device (SQUID) magnetometer to determine the materials' superconducting properties in addition to their compositional homogeneity through determination of T_c and the sharpness of the diamagnetic curves (Fig. 1). Samples prepared for x-ray diffraction were typically ∼1.5 g, while the samples intended for neutron diffraction were ∼4.5 g.

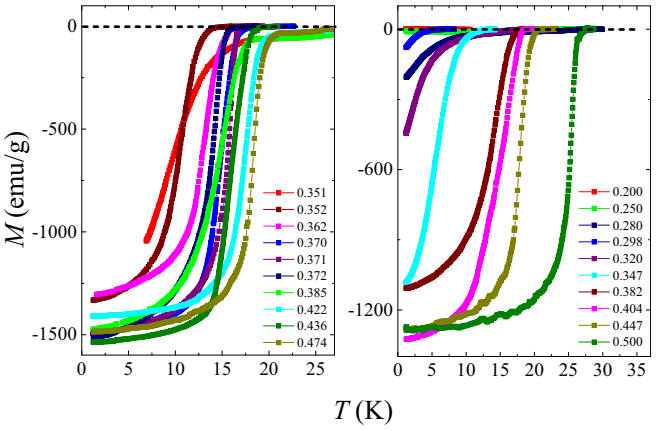

FIG. 1. The superconducting transitions for all measured powders. Magnetization normalized to the mass of the samples used for neutron diffraction (left) and x-ray diffraction (right). All samples show either bulk superconductivity or are nonsuperconducting. The slight variation in diamagnetic response is consistent with small FeAs impurities seen in diffraction patterns.

B. Sample characterization

Diffraction data were collected using the time-of-flight (TOF) neutron powder diffractometer POWGEN at the Spallation Neutron Source (SNS) of Oak Ridge National Laboratory (ORNL) and the high-resolution synchrotron x-ray beam line 11BM-B of the Advanced Photon Source (APS) at Argonne National Laboratory (ANL). Data were collected between 4 K and room temperature on warming. The obtained powder diffraction patterns were used with the Rietveld analysis method as implemented in the GSAS and EXPGUI software suite in order to perform detailed magnetic and nuclear structural analyses [27,28]. Back-to-back exponentials convoluted with a pseudo-Voigt and microstrain broadening were used to model the TOF peak shape profile [29]. A pseudo-Voight peak shape profile function 3 was used to model the data obtained from the synchrotron.

III. RESULTS AND DISCUSSION

A. C_4 magnetic phase

Recently, we have detailed the determination of the magnetic C_4 phase in a series of hole-doped 122 materials: $Ba_{1-x}Na_xFe_2As_2$, $Ba_{1-x}K_xFe_2As_2$, and $Sr_{1-x}Na_xFe_2As_2$ [12,20,30,31]. In these reports, we characterized the C_4 phase by an abrupt first-order reentrance at temperatures $T < T_N$ to the tetragonal $I4/mmm$ structure from within the well-known antiferromagnetically ordered orthorhombic $Fmmm$ structure. This structural transition is coupled to a magnetic transition where the previously in-plane Fe-site moments rotate to be colinear to the c axis forming a double-**Q** magnetic structure with P_C4_2/ncm magnetic space group [31–33].

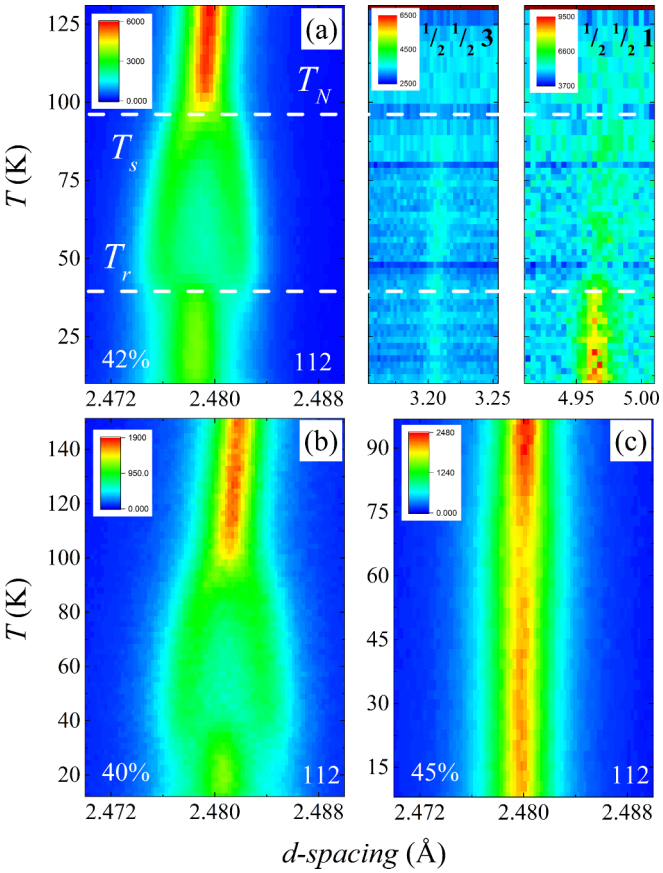

FIG. 2. (a) Diffractograms of the 112 nuclear peak and the magnetic $\frac{1}{2}\frac{1}{2}1$ and $\frac{1}{2}\frac{1}{2}3$ peaks for the $Ca_{0.58}Na_{0.42}Fe_2As_2$ sample. Diffractograms of the 112 peak for the (b) $x = 0.40$ and (c) 0.45 samples. The diffractograms of the nuclear peak and magnetic peaks were compiled from x-ray (11BM-B) and neutron (POWGEN) diffraction patterns, respectively.

Figure 2(a) shows diffractograms of the 112 nuclear peak and the $\frac{1}{2}\frac{1}{2}1$ and $\frac{1}{2}\frac{1}{2}3$ magnetic peaks for $Ca_{0.58}Na_{0.42}Fe_2As_2$ (all peaks indexed using the tetragonal symmetry of the room-temperature structure). By monitoring the temperature dependence of these three peaks, it is possible to distinguish between the two structural symmetries and three magnetic phases. In Fig. 2(a), the typical paramagnetic (PM) C_4 to AFM C_2 transition for the 42% sample is seen. At $T = T_n = T_s \approx$ 105 K, the 112 reflection splits into two distinct reflections (the 202 and 022), indicating a structural transition to the orthorhombic phase. Simultaneously, magnetic scattering can be seen at the previously background equivalent $\frac{1}{2}\frac{1}{2}3$ and $\frac{1}{2}\frac{1}{2}1$ positions—indicating the coupled magnetic/structural transition from the PM tetragonal phase to the AFM orthorhombic phase. The same behavior can be seen in Figs. 2(b) and 2(c) at ≈104 K and ≈89 K for the 40% and 45% samples, respectively. The 45% sample is near the edge of the C_2 dome and therefore exhibits a reduced orthorhombic distortion in the C_2 phase. The orthorhombic splitting cannot be fully resolved in the x-ray diffraction data and instead manifests as a slight broadening of the 122 peak below $T_n \approx 89$ K. At lower temperatures (≈ 38 K), the peak sharpens again, indicating the return to C_4 symmetry.

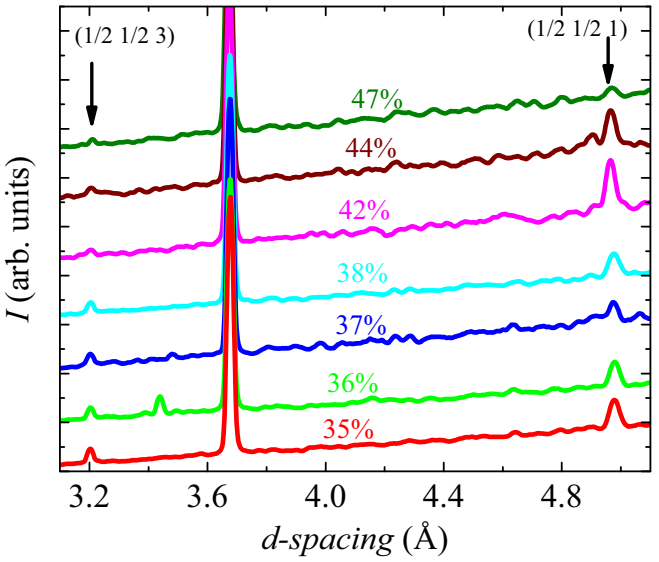

FIG. 3. Neutron diffraction patterns collected on POWGEN at 10 K for a series of compositions near the C_4 dome. Indicated with arrows are the $\frac{1}{2}\frac{1}{2}3$ and $\frac{1}{2}\frac{1}{2}1$ magnetic reflections. Patterns are arbitrarily offset to aid in visual comparison.

As the temperature is decreased below T_N, at $T \leqslant 45$ K the 42% sample's split 112 nuclear peak undergoes a sudden ($\Delta T \sim 10$ K) return to a single reflection. During the same temperature range, the $\frac{1}{2}\frac{1}{2}1$ magnetic peak gains more than a factor of three in scattering intensity. Throughout $12 < T <$ 45 K, the $\frac{1}{2}\frac{1}{2}1$ peak continues to gain intensity while the $\frac{1}{2}\frac{1}{2}3$ reflection shows little temperature dependence. This behavior is indicative of the above-described spin reorientation, where the magnetic moments on the Fe sites align along the c axis. This coupled structural/magnetic transition is characteristic of the magnetic C_4 phase and is observed for all compositions of $Ca_{1-x}Na_xFe_2As_2$ with $0.40 \leqslant x \leqslant 0.45$ in our samples.

Shown in Fig. 3 are neutron powder diffraction patterns collected at 10 K in the d-spacing range of the two magnetic reflections ($\frac{1}{2}\frac{1}{2}1$ and $\frac{1}{2}\frac{1}{2}3$). For samples with $x \leqslant 0.38$, the typical C_2 magnetism is observed, while for the $x = 0.42$ and 0.44 samples, the C_4 structure appears—clear from the increased relative intensity of the $\frac{1}{2}\frac{1}{2}1$ peak compared to lower compositions despite the expected suppression of the magnetic moment with increased doping. Interestingly, for the 47% sample, the C_2 magnetism returns, indicating that the C_4 dome is buttressed at both higher and lower concentrations by the standard AFM stripe magnetism. While not observed in $Ba_{1-x}Na_xFe_2As_2$, we recently reported a similar behavior in $Sr_{1-x}Na_xFe_2As_2$ and $Ba_{1-x}K_xFe_2As_2$ [12,14,20,31]. The significance of this reentrance in composition space will be discussed in Sec. III C.

B. Reentrance of AFM C_2

A notable feature of the diffractograms shown in Fig. 2 is the apparent broadness of the 112 peak at low temperatures as compared to the peak in the PM tetragonal phase. Previously, we reported a similar behavior in $Ba_{1-x}Na_xFe_2As_2$ which was attributed to a finite percentage of the sample remaining in the orthorhombic phase [12]. However, as will be shown, here

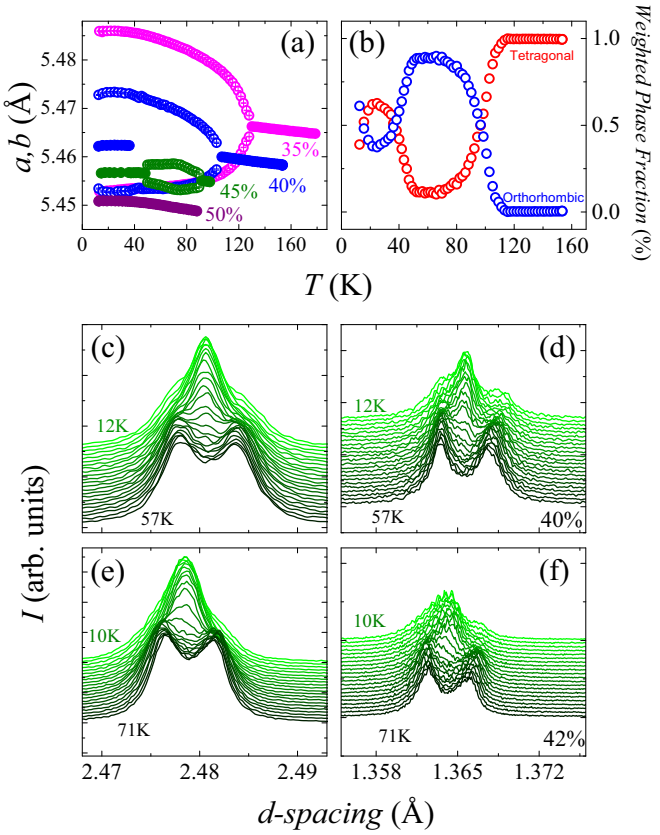

FIG. 4. (a), (b) Lattice parameters of the $x = 0.35,0.40,0.45,0.50$ samples extracted from Rietveld refinements. (a) The a lattice parameter for the tetragonal phases is indicated by filled symbols and has been scaled by a factor of $\sqrt{2}$ to aid in visual comparison. (b) The refined phase fraction of the tetragonal (red) and orthorhombic (blue) phases in a mixed phase refinement for the 40% sample. Waterfall plots showing the temperature dependence of the (c), (e) 112 and (d), (f) 220 nuclear peaks of the 40% and 42% samples, respectively.

the broadness is caused in part by a more complicated phase diagram in the $Ca_{1-x}Na_xFe_2As_2$ material.

Figure 4(a) shows the refined a and b lattice parameters for a series of compositions near the C_4 dome. For the 40% sample, the presence of both tetragonal and orthorhombic lattice parameters below T_r results from a mixed phase refinement. As shown in Figs. 4(c) and 4(d), the orthorhombic 202 and 022 (200 and 020) peaks are always present even to base temperature. Therefore, as in $Ba_{1-x}Na_xFe_2As_2$, for $T < T_r$, $Ca_{0.60}Na_{0.40}Fe_2As_2$ has domains of both C_4 and C_2 symmetries.

However, the intensity of the orthorhombic peaks does not monotonically decrease or remain constant as should be expected for the case of mixed phases due to either chemical inhomogeneity or intrinsic phase separation. Instead, for $T < 20$ K, the intensities of the orthorhombic peaks are seen to increase while the central tetragonal peak decreases [Figs. 4(c) and 4(d)]. Extracting the weighted phase fraction from mixed phase refinements of the 40% sample [Fig. 4(b)], the sample is seen to begin returning to the orthorhombic symmetry from within the C_4 phase. Between 21 K (the maximum phase fraction of C_4) and 12 K (lowest measured temperature), the phase fraction of the C_2 phase changes from 37% to 62%; meanwhile, the C_4 phase drops from being the majority phase at 63% to the minority phase at 38%. Similar behavior is also seen in the 42% sample [Figs. 4(e) and 4(f)]; however, less of the sample exhibits this phase reentrance and so it is not possible to perform reliable and stable mixed phase refinements. Nonetheless, qualitatively the behavior of these two compositions is similar with a reentrance of part of the sample to the C_2 symmetry from within the C_4 phase.

It is important to note that this is a true second reentrance to the C_2 structure and not an artifact born of chemical inhomogeneity; the commensurate shift in opposite directions of the two phases' weighted fractions indicates that the C_4 phase is undergoing another phase transition (characterized as T_{r_2}) back to the C_2 symmetry. Interestingly, T_{r_2} occurs simultaneous to the superconducting transition T_c, within the resolution of our measurements for the 40% sample. A similar combined magnetic, structural, and superconducting transition for $Ba_{0.74}K_{0.26}Fe_2As_2$ has been reported and this behavior indicates the strong competition between superconductivity and the magnetic C_4 phase [14,31].

While such a C_2 reentrance has been reported in $Ba_{1-x}K_xFe_2As_2$ (Ref. [31]) and its significance discussed (Ref. [14]), it has not been reported in any other 122 system as far as the authors of this paper are aware. It is not obvious why $Ca_{1-x}Na_xFe_2As_2$ and $Ba_{1-x}K_xFe_2As_2$ should show C_2 reentrance, while $Ba_{1-x}Na_xFe_2As_2$ and $Sr_{1-x}Na_xFe_2As_2$ do not. Though $Ba_{1-x}K_xFe_2As_2$ is notable for the brevity in composition and temperature space of the C_4 phase—indicating its relative instability to the C_2 phase—in $Ca_{1-x}Na_xFe_2As_2$, the C_4 phase has a relatively robust extent in phase space. The compositional range of C_4 in $Ca_{1-x}Na_xFe_2As_2$ ($\Delta x \sim 0.05$) is comparable to that found in $Ba_{1-x}Na_xFe_2As_2$. Yet, to date, no such reentrance is found for $Ba_{1-x}Na_xFe_2As_2$ despite several careful studies [12,34]. Therefore, this reentrant C_2 is likely born of more subtle effects and warrants further study.

Interestingly, careful inspection of the lattice parameters and peak positions at the C_4 transition in the mixed phase compositions reveals remarkably little change in the lattice parameters between the standard C_2 phase and the coexistent C_2 phase (Fig. 4). Should the mixed phase states be due to a chemical homogeneity, then it should be expected that the remnant portion of the sample in the C_2 phase would exhibit a greater orthorhombic distortion ostensibly being of lower Na concentration. However, as seen in Fig. 4(a), the a and b lattice parameters of the C_2 phase across the C_4 transition are nearly constant, indicating the possibility that it is not some compositionally distinct portion of the sample which is remaining C_2, but that some other effect must be influencing the phase behavior.

In Ref. [31], we reported a similar behavior in the $Ba_{1-x}K_xFe_2As_2$ compound and attributed the extra influence as due to possible localized defects in parts of the sample. Since then, theory has shown that impurity scattering can play a significant role in the stabilization of the C_4 phase [17]. In their work, Hoyer *et al.* show that intraband electron scattering due to crystallographic defects stabilize the C_4 phase at lower doping concentrations—at the beginning of the C_4 dome. However, no such effect is found on the higher doped side of the dome, in agreement with our observation of mixed phase samples at the onset of C_4 in composition but

TABLE I. Fitted composition and structural and magnetic transition temperatures with errors shown in parentheses. Fit compositions were determined through the use of a Vegard's law such as behavior of the a lattice parameter (see Ref. [20] for a description of the procedure used for sample composition determination). Critical temperatures (T_c, T_s, T_N, T_r, and T_{r_2}) were determined using a consistently applied methodology (see text for details).

x_{fit}	T_c	T_N	T_s	T_r	T_{r_2}
		Neutron data			
0.35(2)	11(1)	119(3)	119(5)		
0.35(2)	12(1)				
0.36(2)	14(1)				
0.37(2)	16(1)	113(5)	115(5)		
0.37(2)	16(1)	110(4)	112(5)		
0.38(2)	16(1)	108(4)	106(5)		
0.42(2)	18(1)	105(4)		40(4)	12(4)
0.44(2)	17(1)	101(4)		52(4)	
0.47(2)	19(1)				
		X-ray data			
0.20(2)					
0.25(2)					
0.30(2)	3(1)				
0.32(2)	5(1)				
0.35(2)	10(2)		126(4)		
0.38(2)	17(1)		109(4)		
0.40(2)	18(2)		104(4)	24(4)	18(2)
0.42(2)	18(1)		105(4)	40(5)	
0.45(2)	19(1)		89(4)	38(5)	
0.50(2)	26(1)				

not at higher concentrations. While, admittedly, it is difficult to decouple such defects from chemical inhomogeneity (e.g., inhomogeneity in the distribution of the dopant atom), our data indicate that there is another variable other than composition which also affects the phase behavior of the material. Further experimental work is needed to determine the exact role defects play in stabilizing the C_4 through either irradiation (as suggested in Ref. [17]), cosubstitution with an isovalent atom, or mechanically introduced crystallographic defects.

C. Phase diagram

Table I lists the transition temperatures of all measured samples. In order to consistently determine the critical temperatures across all samples (considering many have competing order parameters), the typical power-law fitting method used to determine T_N and T_s was eschewed [30,35–37]. Instead, the methodology described in Ref. [20] was employed. Critical temperatures were determined by comparing linear fits of the order parameter immediately before and after the transition. The order parameters used were magnetization (M), magnetic moment (m), and orthorhombic distortion [$\delta = (a-b)/(a+b)$]. While the former two were used for T_c and T_N, respectively, the latter was used for T_s as well as T_{r_2}. For T_r, the collapse of δ was used. In this manner, modifications to the expected power-law behavior due to the presence of a third (and fourth) phase transition, specifically in samples exhibiting T_r's, could be mitigated and a consistent method used across all transitions and samples.

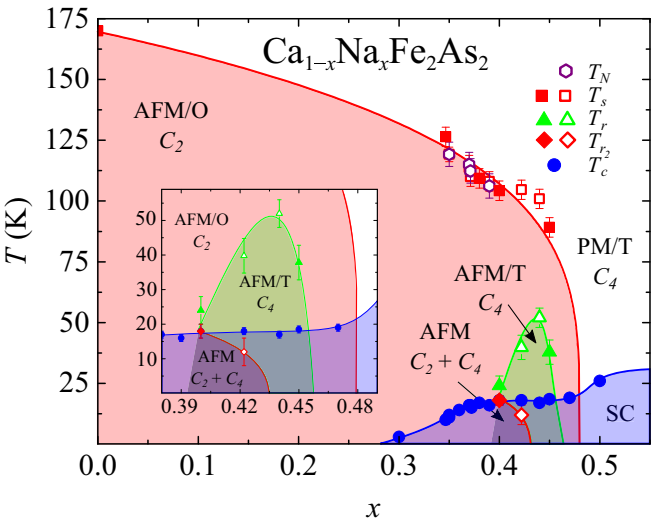

FIG. 5. Phase diagram of $Ca_{1-x}Na_xFe_2As_2$. Filled and open symbols are transitions determined from x-ray and neutron data, respectively. The parent compound's transition temperature was taken from Ref. [38]. The red, blue, and green shaded areas represent the AFM orthorhombic, superconducting, and AFM tetragonal phases, respectively. The shaded region indicates phase coexistence between the C_4 phase and a reentrant C_2 phase. Coincident structural and magnetic transitions are represented for each phase by a solid line. Inset: an enlarged view showing details of the C_4 dome.

Figure 5 shows the graphical representation of Table I forming a phase diagram for $Ca_{1-x}Na_xFe_2As_2$. While sharing general features with the previously reported $Ca_{1-x}Na_xFe_2As_2$ phase diagrams (Refs. [22] and [21]), our use of fine steps in composition, specifically towards the edge of the C_2 dome, reveals a C_4 dome in this hole-doped $CaFe_2As_2$ system. The C_4 phase first appears at $x \sim 0.40$ at $T = 24$ K and continues in composition space until $x \sim 0.47$ where the AFM C_2 phase returns, describing a C_4 dome with $\Delta x = 0.05$ in composition. The compositional dependence of T_r in this range is roughly parabolic with a maximum T_r of 52 K at $x = 0.44$, which then decreases with further doping. For $0.47 < x < 0.50$, magnetism and the accompanying structural distortion are completely suppressed, describing the closing of the C_2 dome.

As previously reported, superconductivity is first seen at $x = 0.30$, where it monotonically rises with composition until reaching 26 K for the 50% sample—the highest composition measured in this study. Interestingly, at the onset in the composition of the C_4 phase, T_c is seen to plateau, exhibiting no composition dependence (within the resolution of our measurements) over $0.40 \leqslant x \leqslant 0.45$. This suppression of T_c by C_4 indicates the strong competition between the C_4 phase magnetic ordering and superconductivity as recently suggested in a first-principles calculations report of the C_4 phase [15].

The previously discussed reentrant C_2 phase is visible in Fig. 5 as a shaded region. Qualitatively, the behavior of this mixed phase region is very similar to that observed previously in Refs. [14] and [31] and explained theoretically in Ref. [15] for the $Ba_{1-x}K_xFe_2As_2$ material. It is noteworthy that all three systems show a decreasing T_{r_2} with increasing composition resulting in the reentrance only affecting the lower doped side of the C_4 dome. Furthermore, we find that

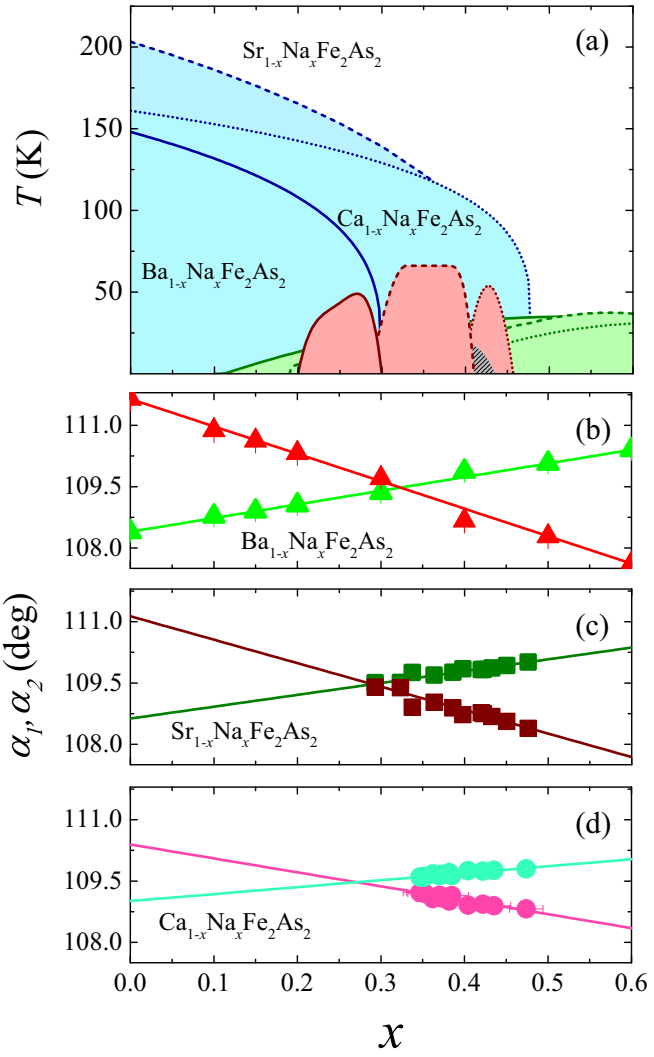

FIG. 6. (a) Phase diagrams of the three Na^+-doped 122 systems overlaid. The solid, dashed, and short-dashed lines correspond to the $Ba_{1-x}Na_xFe_2As_2$, $Sr_{1-x}Na_xFe_2As_2$, and $Ca_{1-x}Na_xFe_2As_2$ phase boundaries, respectively. The blue, red, and green shaded regions correspond to the AFM C_2, AFM C_4, and SC phases, respectively. The composition dependence of the FeAs layer tetrahedral angles at 10 K for (b) $Ba_{1-x}Na_xFe_2As_2$, (c) $Sr_{1-x}Na_xFe_2As_2$, and (d) $Ca_{1-x}Na_xFe_2As_2$. Values for the angles of $Ba_{1-x}Na_xFe_2As_2$ and $Sr_{1-x}Na_xFe_2As_2$ were taken from Refs. [30] and [20], respectively.

$T_{r_2} \leqslant T_c$—consistent with recent reports which have suggested the C_4 phase's doubly gapped Fermi surface competes more strongly with superconductivity than the singly gapped C_2 phase [15,16].

D. Comparison of hole-doped 122's

1. *Phase diagrams and extent of the C_4 phase*

Figure 6(a) plots the phase diagrams of $Ba_{1-x}Na_xFe_2As_2$, $Sr_{1-x}Na_xFe_2As_2$, and $Ca_{1-x}Na_xFe_2As_2$ on shared axes (the former two compounds' phase diagrams are generated from data we reported in Refs. [12] and [20], respectively). As noted in Ref. [39], the T_N of the parent compounds is nonmonotonic going up the alkali-earth metal group from Ba to Sr to Ca with T_N of 140, 210, and 170 K, respectively [30,38,40]. Setting aside the composition dependence, it is somewhat unsurprising that the maximum T_r for each system appears to scale with T_N going from 45 to 65 to 52 K for Ba, Sr, and Ca [20,30,41].

Naively, the scaling of the T_N of the parent compound with T_r seems reasonable, assuming a higher magnetic ordering temperature would require a larger amount of charge doping to disrupt. This would then extend the C_2 dome out to higher compositions and, consequently, allow for a more fully formed C_4 dome. However, several features of this comparison dispute this explanation. Unexpectedly, though T_N of the parent decreases between Sr and Ca, the extent of the C_2 dome is nearly the same (with a shared critical composition of $x \sim 47\%$). Furthermore, despite this and the higher T_N of $SrFe_2As_2$, $Ca_{1-x}Na_xFe_2As_2$ does not exhibit C_4 reentrant behavior until significantly higher dopant concentrations ($x \sim 0.29$ for $Sr_{1-x}Na_xFe_2As_2$ compared to $x \sim 0.40$ for $Ca_{1-x}Na_xFe_2As_2$), indicating a more complex relationship between the parent compound's T_N and the effect of Na^+ doping.

As discussed in Ref. [39], the nonmonotonic behavior of the T_N between the three parent compounds as well as the itinerant electronic behavior indicates that the changes in the magnetic and electronic behavior must be due to structural changes in the material. Such considerations can be extended to these three charge doped systems due to the direct correspondence at any given dopant concentration to a similar charge doping in all systems. The significant difference between the three systems for a given Na^+ concentration is the average size of the A-site ion, which will impact the overall structure of the unit cell as well as the important internal bonding parameters and affect the differences seen in Figs. 6(b)–6(d). These effects will be the focus of Sec. III D 3.

2. *Structure and magnetism*

The observation of the C_4 phase in $Ca_{1-x}Na_xFe_2As_2$ makes it the fourth member of the hole-doped 122 family to exhibit this phase, demonstrating that it is an intrinsic (rather than coincidental) feature of these materials. Considering the three Na^+-doped compounds ($Ba_{1-x}Na_xFe_2As_2$, $Sr_{1-x}Na_xFe_2As_2$, and $Ca_{1-x}Na_xFe_2As_2$) allows for the influence of structural changes on the formation of the C_4 phase to be isolated from the effects of charge doping.

The ionic radius of the A site in AFe_2As_2 decreases from 1.42 to 1.26 to 1.12 Å as the A-site ion goes up the alkaline-earth metals from Ba to Sr to Ca, respectively [42]. This decrease should be expected to cause a contraction of the unit-cell volume, which in turn will tune the magnetic properties by changing the Fe-Fe distances as well as the Fe_2As_2 interlayer spacings. Figure 7(a) shows the unit-cell volume (V) of the three Na^+-doped compounds. As expected, V decreases from $BaFe_2As_2$ to $SrFe_2As_2$ to $CaFe_2As_2$ in nearly equal steps of approximately -6.5% and -7.0%, respectively.

However, this contraction is anisotropic. Figures 7(b) and 7(c) show the a_{tet} and c lattice parameters. While both contract as the A-site ion is moved up the group, the c axis is significantly more sensitive, changing by -5% for each step up compared to approximately -1% for the a_{tet} direction. This is quantitatively measured with the anisotropy ratio c/a [Fig. 7(d)], which steadily decreases from Ba to Ca. This

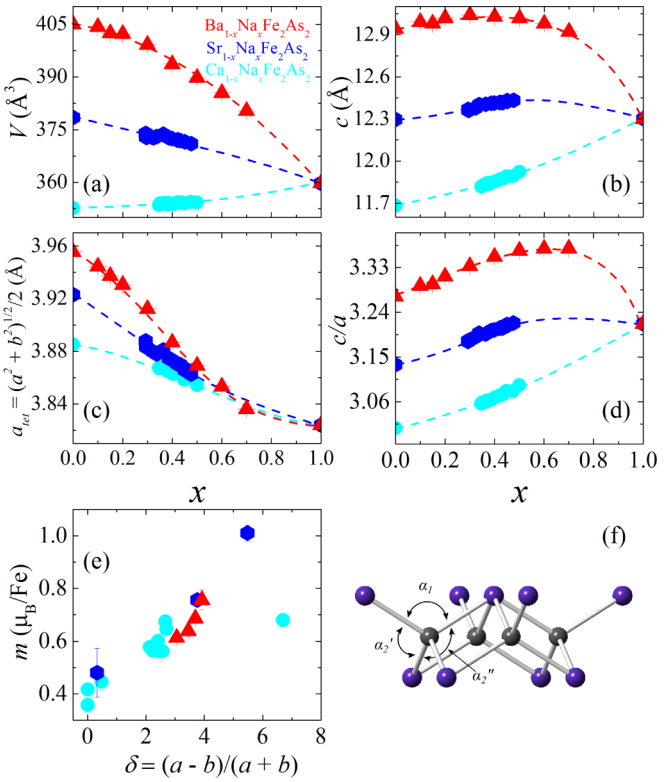

FIG. 7. Compositional dependence of the unit cell: (a) volume, (b) c axis, (c) a_{tet} direction, and (d) c/a ratio for the three Na^+-doped 122 systems at 300 K. (e) The refined magnetic moment plotted as a function of the orthorhombic order parameter δ (where δ has been scaled by a factor of 10^3) for data collected at 10 K. (f) The Fe_2As_2 layer with the α_1 and two α_2 angles indicated. Data for $Ba_{1-x}Na_xFe_2As_2$ and $Sr_{1-x}Na_xFe_2As_2$ were taken from Refs. [30] and [20], respectively.

anisotropic contraction of the unit cell should be expected to significantly affect the geometry of the Fe_2As_2 layers and the Fe-Fe spacing, both in and out of plane, as will be discussed in Sec. III D 3.

The strong magnetoelastic coupling in the 122 materials is well characterized at this point both experimentally and theoretically [5,10,11,43–45]. In Fig. 7(e), the magnetic order parameter (m) is plotted as a function of the structural order parameter (δ) for all three systems at base temperature. Remarkably, despite the differences in the compounds' C_2 phase composition dependence and absent any scaling, the three systems appear to fall on the same $m(\delta)$ curve. As expected, $m(\delta)$ increases monotonically between $0 \leqslant \delta \leqslant 5.5$ [where $m(0)$ accounts for AFM C_4 samples], indicating the relationship between the magnitude of the structural distortion and the strength of the magnetic ordering.

Whether the two order parameters are related linearly or quadratically has long been debated [37]. While Fig. 7 seems to indicate a quadratic relationship for $\delta < 5.5$, the quality of the data does not afford much certainty. However, it is interesting to note the similarity between the three systems. In a linear approximation (as suggested in Ref. [46] and derived explicitly in Ref. [43]), $\delta(m)$ has the form $\delta = \alpha m$ where α is a constant related to the strength of the magnetoelastic coupling, the shear

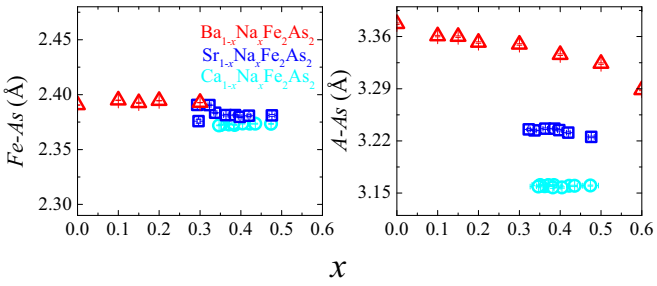

FIG. 8. Fe-As (left) and A-Fe (right) bond lengths of the three Na-doped 122 materials at 10 K.

modulus, and the chemical doping. That all three systems fall on the same curve indicates the similarity between these important parameters despite the different parent compounds.

For $\delta > 5.5$, m decreases with increasing δ. This region corresponds to the underdoped $Ca_{1-x}Na_xFe_2As_2$ samples and is similar to the unexpected decrease in m seen in the parent compounds between $SrFe_2As_2$ and $CaFe_2As_2$. This is likely related to the nonmonotonic behavior of T_N and m as a function of unit-cell volume for $Ba_{1-x}Sr_xFe_2As_2$ and $Sr_{1-x}Ca_xFe_2As_2$ reported in Ref. [39]. Unfortunately, due to the focus of the present study on compositions towards the edge of the C_2 dome, we do not have data on significantly underdoped compositions leaving a large gap between the maximum $m_{max}(\delta)$ and δ_{max} limiting our ability to fit the curve in this region.

3. *Internal parameters*

As shown in Fig. 7(d), there is a significant decrease in the lattice anisotropy among the three parent compounds which persists even to our highest measured Na concentrations. It should be expected then that the Fe_2As_2 layers (which are characterized by the Fe-Fe and Fe-As bond lengths as well as the As-Fe-As angles [Fig. 7(f)]) have significantly different geometries in these three materials.

Recently, we suggested the importance of the Fe_2As_2 layers' bonding parameters to the stabilization of the C_4 phase [20]. In $Sr_{1-x}Na_xFe_2As_2$, the C_4 phase was found to occur in a small range of As-Fe-As bond angles where the $FeAs_4$ approached perfect tetrahedra. We suggested that the return locally to a higher symmetry in the Fe_2As_2 layers might create an electronic instability which contributes to the recovery of magnetic degeneracy and a consequent return to C_4 symmetry. It is then informative to look at all three Na-doped systems and quantify how these bond angles change with structure and how this relates to the observed phase diagrams.

Figure 8 shows the Fe-As and A-As bond lengths for the three Na-doped materials. As reported for $Sr_{1-x}Na_xFe_2As_2$, the Fe-As bond length is nearly constant across all measured Na concentrations and even, strikingly, across the different materials. However, as shown in Figs. 7(a) and 7(b), there is a significant reduction of the unit-cell volume and of the c axis across the three materials which must result in changes to the internal bonding parameters. Interestingly, this contraction does not affect the robust Fe-As bond, but is instead compensated for in the A-site to As bond length (Fig. 8), which contracts significantly between the three systems following the trend seen in V and the c axis.

The Fe-Fe bond length is proportional to the a lattice parameter due to the Fe atom's location on a special crystallographic site. Therefore, the previously discussed ~1% contraction of the a axis between parent compounds corresponds to an identical contraction of the Fe-Fe distance in response to the smaller A-site ion. On the other hand, the effects of Na^+ doping on the Fe-Fe bond have been discussed previously in Ref. [30], and result in the reduction of antibonding between neighboring Fe and therefore a contraction of Fe-Fe bond distance. As the A site is changed between the systems from Ba to Ca, the Fe-Fe bond length contracts. Furthermore, as Na is doped into each parent compound, the Fe-Fe bond length also contracts. The combination of these two effects leads to the decreases in a seen in Fig. 7(c) and the latter effect causes the severely reduced a seen in the end compound $NaFe_2As_2$.

The sum of these effects indicates that the decreasing c/a ratio from $BaFe_2As_2$ to $SrFe_2As_2$ to $CaFe_2As_2$ has different manifestations along the different crystallographic directions for the Fe_2As_2 layers. The large contraction along c is a result of A-As bond lengths leaving the FeAs bond unchanged, while the contraction along a directly corresponds to a reduction in spacing between Fe atoms in the Fe_2As_2 layer's square planar Fe sublattice. As seen in the lower panels of Fig. 6, the result is a change in the As-Fe-As angles α_1 and α_2. $BaFe_2As_2$, which has the largest c/a ratio, also has the largest splitting between the two angles, $\Delta\alpha = |\alpha_1 - \alpha_2| = 3.20^\circ$. $\Delta\alpha$ decreases in $SrFe_2As_2$ and $CaFe_2As_2$ to 2.58° and 1.43°, respectively.

As Na^+ is doped into these materials, the two As-Fe-As angles begin to converge. The Fe-Fe contraction and Fe-As rigidity drive the wider α_1 angle to close and the smaller α_2 angle to open until the two angles cross at the perfect tetrahedral angle (109.46°) at $x = 0.32$, 0.29, and 0.27, for $Ba_{1-x}Na_xFe_2As_2$, $Sr_{1-x}Na_xFe_2As_2$, and $Ca_{1-x}Na_xFe_2As_2$, respectively. Upon further doping, the angles separate with $\alpha_1 < \alpha_2$.

At various times, the role of α_1 and α_2 as important parameters in determining the electronic structure of these materials has been explored [47–51]. The bond angles are closely related to the pnictogen height and determine the overlap between the pnictogen's p orbitals and the Fe sites' $3d$ orbitals. In Ref. [49], first-principles calculations predict that the Fermi surface becomes more degenerate as $\Delta\alpha \to 0$. It is possible that the recipe for C_4 involves balancing this return to a higher-symmetry FS, with the needed isotropy between the size of the hole and electron FS sheets known to be necessary to stabilize C_4 [12]. Such a description would explain why C_4 is seen only over a short range of compositions where these two conditions are met within the C_2 dome. However, most reports using first-principles calculations to study the importance of the Fe_2As_2 layer geometry were performed before the discovery of the C_4 phase. It would be useful now to revisit these discussions in light of this phase.

IV. CONCLUSIONS

We report the observation of the magnetic C_4 phase in a fourth member of the hole-doped 122 family of FBS—$Ca_{1-x}Na_xFe_2As_2$—as determined by high-resolution neutron and x-ray diffraction experiments. A C_4 dome is seen for compositions $0.40 \leqslant x \leqslant 0.45$ with a maximum T_r of ~52 K. For higher compositions, $0.45 < x \leqslant 0.47$, only C_2 magnetism is observed describing a C_4 dome which closes before the complete suppression of magnetic ordering. On the low composition side of the C_4 phase, a reentrance to the C_2 phase is observed which coincides with the arrival of superconductivity in the $x = 0.40$ sample.

Compared to the previous C_4 containing 122's, we report a phase diagram which has a mix of the previously discrete features, such as the separated C_2 and C_4 domes seen only in $Sr_{1-x}Na_xFe_2As_2$ and the reentrant C_2 only detected in $Ba_{1-x}K_xFe_2As_2$. These observations seem to indicate important subtle structural effects as the controlling factors for the formation of the C_4 phase which are considered in a comparison of the three Na^+-doped materials—$Ba_{1-x}Na_xFe_2As_2$, $Sr_{1-x}Na_xFe_2As_2$, and $Ca_{1-x}Na_xFe_2As_2$.

An anisotropic contraction of the unit cell is observed upon changing the A site from Ba to Sr to Ca caused by a markedly larger sensitivity of the c axis to the A-site ion than the a axis. By comparing the internal parameters, it is found that the Fe-Fe and Fe-As bond lengths are robust to changes in the A site with the consequent lattice response resulting from A-Fe bond lengths and As-Fe-As bond angles. An intriguing correlation between the As-Fe-As bond angle and the C_4 phase is reported where for all three Na^+-doped materials the C_4 phase occurs in close proximity to the perfect tetrahedral angle. We suggest the possibility of this local return to higher symmetry as a factor in the C_2 /C_4 structure instability and advocate for a revisit of the first-principle studies of the Fe_2As_2 layer geometry's effect on the 122's phase stability.

ACKNOWLEDGMENTS

The work at the Materials Science Division of Argonne National Laboratory was supported by the U.S. Department of Energy, Office of Science, Materials Sciences and Engineering Division. Research conducted at ORNL's High Flux Isotope Reactor and Spallation Neutron Source was sponsored by the Scientific User Facilities Division, Office of Basic Energy Sciences, U.S. Department of Energy. Use of the Advanced Photon Source at Argonne National Laboratory was supported by the U.S. Department of Energy, Office of Science, Office of Basic Energy Sciences under Contract No. DE-AC02-06CH11357. The authors thank A. Huq and P. Whitfield for providing help during experimental data collection and analysis.

[1] Y. Kamihara, H. Hiramatsu, M. Hirano, R. Kawamura, H. Yanagi, T. Kamiya, and H. Hosono, J. Am. Chem. Soc. **128**, 10012 (2006).

[2] D. N. Basov and V. Chubukov, Nat. Phys. **7**, 272 (2011).

[3] M. Rotter, M. Tegel, D. Johrendt, I. Schellenberg, W. Hermes, and R. Pöttgen, Phys. Rev. B **78**, 020503 (2008).

[4] A. D. Christianson, E. A. Goremychkin, R. Osborn, S. Rosenkranz, M. D. Lumsden, C. D. Malliakas, I. S. Todorov,

H. Claus, D. Y. Chung, M. G. Kanatzidis, R. I. Bewley, and T. Guidi, Nat. Lett. **456**, 930 (2008).
[5] S. Avci, O. Chmaissem, E. A. Goremychkin, S. Rosenkranz, J.-P. Castellan, D. Y. Chung, I. S. Todorov, J. A. Schlueter, H. Claus, M. G. Kanatzidis, A. Daoud-Aladine, D. Khalyavin, and R. Osborn, Phys. Rev. B **83**, 172503 (2011).
[6] H. H. Kuo, M. C. Shapiro, S. C. Riggs, and I. R. Fisher, Phys. Rev. B **88**, 085113 (2013).
[7] J. H. Chu, H. H. Kuo, J. G. Analytis, and I. R. Fisher, Science **337**, 710 (2012).
[8] S. Kasahara, H. J. Shi, K. Hashimoto, S. Tonegawa, Y. Mizukami, T. Shibauchi, K. Sugimoto, T. Fukuda, T. Terashima, A. H. Nevidomskyy, and Y. Matsuda, Nature (London) **486**, 382 (2012).
[9] M. Yi, D. Lu, J.-H. Chu, J. Analytis, A. Sorini, A. Kemper, B. Moritz, S.-K. Mo, R. Moore, M. Hashimoto, W. Lee, Z. Hussain, T. Devereaux, I. Fisher, and Z.-X. Shen, Proc. Natl. Acad. Sci. USA **108**, 6878 (2011).
[10] C. Dhital, Z. Yamani, W. Tian, J. Zeretsky, A. S. Sefat, Z. Wang, R. J. Birgeneau, and S. D. Wilson, Phys. Rev. Lett. **108**, 087001 (2012).
[11] R. M. Fernandes, A. E. Böhmer, C. Meingast, and J. Schmalian, Phys. Rev. Lett. **111**, 137001 (2013).
[12] S. Avci, O. Chmaissem, J. M. Allred, S. Rosenkranz, I. Eremin, A. V. Chubukov, D. E. Bugaris, D. Y. Chung, M. G. Kanatzidis, J.-P. Castellan, J. A. Schlueter, H. Claus, D. D. Khalyavin, P. Manuel, A. Daoud-Aladine, and R. Osborn, Nat. Commun. **5**, 3845 (2014).
[13] J. M. Allred, K. M. Taddei, D. E. Bugaris, M. J. Krogstad, S. H. Lapidus, D. Y. Chung, H. Claus, M. Kanatzidis, D. Brown, J. Kang, R. Fernandes, I. Eremin, S. Rosenkranz, O. Chmaissem, and R. Osborn, Nat. Phys. **12**, 493 (2016).
[14] A. E. Böhmer, F. Hardy, L. Wang, T. Wolf, P. Schweiss, and C. Meingast, Nat. Commun. **6**, 7911 (2015).
[15] J. Kang, X. Wang, A. V. Chubukov, and R. M. Fernandes, Phys. Rev. B **91**, 121104 (2015).
[16] M. N. Gastiasoro and B. M. Andersen, Phys. Rev. B **92**, 140506 (2015).
[17] M. Hoyer, R. M. Fernandes, A. Levchenko, and J. Schmalian, Phys. Rev. B **93**, 144414 (2016).
[18] M. H. Christensen, J. Kang, B. M. Andersen, I. Eremin, and R. M. Fernandes, Phys. Rev. B **92**, 214509 (2015).
[19] R. M. Fernandes, S. A. Kivelson, and E. Berg, Phys. Rev. B **93**, 014511 (2016).
[20] K. M. Taddei, J. M. Allred, D. E. Bugaris, S. Lapidus, M. J. Krogstad, R. Stadel, H. Claus, D. Y. Chung, M. G. Kanatzidis, S. Rosenkranz, R. Osborn, and O. Chmaissem, Phys. Rev. B **93**, 134510 (2016).
[21] K. Zhao, Q. Q. Liu, X. C. Wang, Z. Deng, Y. X. Lv, J. L. Zhu, F. Y. Li, and C. Q. Jin, Phys. Rev. B **84**, 184534 (2011).
[22] P. Materne, S. Kamusella, R. Sarkar, T. Goltz, J. Spehling, H. Maeter, L. Harnagea, S. Wurmehl, B. Büchner, H. Luetkens *et al.*, Phys. Rev. B **92**, 134511 (2015).
[23] N. Haberkorn, B. Maiorov, M. Jaime, I. Usov, M. Miura, G. F. Chen, W. Yu, and L. Civale, Phys. Rev. B **84**, 064533 (2011).
[24] J. Dong, H. J. Zhang, G. Xu, Z. Li, G. Li, W. Z. Hu, D. Wu, G. F. Chen, X. Dai, J. L. Luo, Z. Fang, and N. L. Wang, Europhys. Lett. **83**, 27006 (2008).
[25] K. Zhao, Q. Q. Liu, X. C. Wang, Z. Deng, Y. X. Lv, J. L. Zhu, F. Y. Li, and C. Q. Jin, J. Phys. Condens. Matter **22**, 222203 (2010).
[26] G. Wu, H. Chen, T. Wu, Y. L. Xie, Y. J. Yan, R. H. Liu, X. F. Wang, J. J. Ying, and X. H. Chen, J. Phys. Condens. Matter **20**, 422201 (2008).
[27] B. H. Toby, J. Appl. Crystallogr. **34**, 210 (2001).
[28] A. C. Larson and R. B. Von Dreele, *Report No. LAUR 86-748* (Los Alamos National Laboratory, Los Alamos, NM, 2004).
[29] P. W. Stephens, J. Appl. Crystallogr. **32**, 281 (1999).
[30] S. Avci, J. M. Allred, O. Chmaissem, D. Y. Chung, S. Rosenkranz, J. A. Schlueter, H. Claus, A. Daoud-Aladine, D. D. Khalyavin, P. Manuel, A. Llobet, M. R. Suchomel, M. G. Kanatzidis, and R. Osborn, Phys. Rev. B **88**, 094510 (2013).
[31] J. M. Allred, S. Avci, D. Y. Chung, H. Claus, D. D. Khalyavin, P. Manuel, K. M. Taddei, M. G. Kanatzidis, S. Rosenkranz, R. Osborn, and O. Chmaissem, Phys. Rev. B **92**, 094515 (2015).
[32] F. Waßer, A. Schneidewind, Y. Sidis, S. Wurmehl, S. Aswartham, B. Büchner, and M. Braden, Phys. Rev. B **91**, 060505 (2015).
[33] B. P. P. Mallett, Y. G. Pashkevich, A. Gusev, T. Wolf, and C. Bernhard, Europhys. Lett. **111**, 57001 (2015).
[34] L. Wang, F. Hardy, A. E. Böhmer, T. Wolf, P. Schweiss, and C. Meingast, Phys. Rev. B **93**, 014514 (2016).
[35] S. D. Wilson, Z. Yamani, C. R. Rotundu, B. Freelon, E. Bourret-Courchesne, and R. J. Birgeneau, Phys. Rev. B **79**, 184519 (2009).
[36] K. Matan, R. Morinaga, K. Iida, and T. J. Sato, Phys. Rev. B **79**, 054526 (2009).
[37] S. Avci, O. Chmaissem, D. Y. Chung, S. Rosenkranz, E. A. Goremychkin, J. P. Castellan, I. S. Todorov, J. A. Schlueter, H. Claus, A. Daoud-Aladine, D. D. Khalyavin, M. G. Kanatzidis, and R. Osborn, Phys. Rev. B **85**, 184507 (2012).
[38] B. Saparov, C. Cantoni, M. Pan, T. C. Hogan, W. Ratcliff II, S. D. Wilson, K. Fritsch, M. Tachibana, B. D. Gaulin, and A. S. Sefat, Sci. Rep. **4**, 4120 (2014).
[39] K. Kirshenbaum, N. P. Butch, S. R. Saha, P. Y. Zavalij, B. G. Ueland, J. W. Lynn, and J. Paglione, Phys. Rev. B **86**, 060504 (2012).
[40] C. Krellner, N. Caroca-Canales, A. Jesche, H. Rosner, A. Ormeci, and C. Geibel, Phys. Rev. B **78**, 100504 (2008).
[41] X. Wang, J. Kang, and R. M. Fernandes, Phys. Rev. B **91**, 024401 (2015).
[42] R. D. Shannon, Acta Crystallogr. Sect. A **32**, 751 (1976).
[43] R. M. Fernandes and J. Schmalian, Supercond. Sci. Technol. **25**, 084005 (2012).
[44] A. V. Chubukov, M. Khodas, and R. M. Fernandes, Phys. Rev. X **6**, 041045 (2016).
[45] A. Cano, M. Civelli, I. Eremin, and I. Paul, Phys. Rev. B **82**, 020408 (2010).
[46] M. H. Fang, H. M. Pham, B. Qian, T. J. Liu, E. K. Vehstedt, Y. Liu, L. Spinu, and Z. Q. Mao, Phys. Rev. B **78**, 224503 (2008).
[47] C.-H. Lee, A. Iyo, H. Eisaki, H. Kito, M. T. Fernandez-Diaz, T. Ito, K. Kihou, H. Matsuhata, M. Braden, and K. Yamada, J. Phys. Soc. Jpn. **77**, 083704 (2008).
[48] E. Z. Kuchinskii, I. A. Nekrasov, and M. V. Sadovskii, JETP Lett. **91**, 518 (2010).
[49] H. Usui and K. Kuroki, Phys. Rev. B **84**, 024505 (2011).
[50] H. Usui, K. Suzuki, and K. Kuroki, Superconducting Sci. Technol. **25**, 084004 (2012).
[51] T. Miyake, K. Nakamura, R. Arita, and M. Imada, J. Phys. Soc. Jpn. **79**, 044705 (2010).